Journal of Photochemistry & Photobiology, A: Chemistry 462 (2025) 116252

Contents lists available at ScienceDirect

Journal of Photochemistry & Photobiology, A: Chemistry

journal homepage: www.elsevier.com/locate/jphotochem

Enhanced photodegradation of tetracycline by novel porous g-C_3N_4 nanosheets under visible light irradiation

Nothando A. Phakathi *, Shepherd M. Tichapondwa, Evans M.N. Chirwa

Water Utilisation and Environmental Engineering Division, Building 2, South Campus, Department of Chemical Engineering, University of Pretoria, Pretoria 0002, South Africa
Private Bag X20, Hatfield 0028, South Africa

ARTICLE INFO

Keywords:
Advanced oxidation processes
Emerging pollutants
Tetracycline
Semiconductor photocatalysis
Surface modification

ABSTRACT

Harnessing photocatalysis to degrade recalcitrant organic pollutants is a potent solution to addressing water pollution and alleviating energy crisis. Photocatalysts possessing intriguing characteristics such as controllable band gap, efficient visible-light absorption and high photocatalytic activity play a pivotal role in this regard. Herein, porous g-C_3N_4 nanosheets were synthesised via pyrocondensation polymerization with melamine and NH_4HCO_3 and their photocatalytic performance was investigated for degradation of tetracycline. Characterization techniques including XRD, FTIR, SEM, TEM, BET and UV–Vis spectroscopy were employed and revealed that porous g-C_3N_4 nanosheets increased light absorption capacity, provided more reactive sites and suppressed recombination of photogenerated electron-hole pairs, thus enhancing the material's photodegradation efficiency in the degradation of tetracycline. Optimization studies showed that 83 % of tetracycline was removed after 2 h of visible light irradiation using 1 gL^{-1} catalyst loading, an initial concentration of 10 ppm and a solution pH of 7. The catalyst showed remarkable recyclability, retaining its chemical structure and functional properties, with 68 % degradation achieved after 5 cycles. Through radical scavenging experiments, superoxide radicals ($\bullet O_2^-$) and photogenerated hole (h^+) were identified as the primary active species responsible for TC degradation. A plausible photocatalytic mechanism was proposed from these experiments. This study provides a facile, cost effective, eco-conscious and effective approach for incorporating porous hierarchical and 2D nanosheets morphology on g-C_3N_4 to enhance its photocatalytic performance under visible light.

1. Introduction

Innovations in human scientific development have led to the production of pharmaceutical products that are proficient in preventing, treating, and curing diseases, improving the quality of life, and increasing the life expectancy of humans and animals. As a result of these innovations, there is regular consumption of some pharmaceutical products [1]. Owing to the blooming consumption and subsequent excretion of pharmaceutical products, numerous Pharmaceutically Active Compounds (PhACs), recognized as emerging contaminants, have been detected in various environmental matrices such as surface water, groundwater, soil, and water/wastewater treatment plants worldwide [2]. Among the pharmaceutically active compounds detected in water bodies, antibiotics have attracted attention as they have short- and long-term health implications for humans and aquatic species [3]. The increasing detection and transformation of antibiotics in aquatic environments and municipal wastewater effluents have become a global environmental issue. African-based studies on the occurrence of pharmaceuticals in aquatic systems revealed regular detection of nearly 24 antibiotics in surface water, and 14 of these antibiotics were reported in Europe-based studies [4].

Tetracycline (TC) is recognized as one of the commonly used antibiotics worldwide. The continual release of this antibiotic into water bodies has contributed to their persistent presence in the environment [5]. The abundant existence of tetracycline in aquatic systems was reported to have adverse effects on the distribution of microbial communities and contributes to the development of bacterial drug resistance, posing a risk of ecological imbalance [6]. Tetracycline is partially susceptible to degradation through conventional water treatment methods due to its high stability [7]. Human health and environmental concerns associated with the presence of antibiotics in aquatic environments have necessitated their removal from wastewater. Wastewater treatment

* Corresponding author at: P O Box 230, Elukwatini 1192, South Africa.
E-mail addresses: u17381292@tuks.co.za (N.A. Phakathi), shepherd.tichapondwa@up.ac.za (S.M. Tichapondwa), evans.chirwa@up.ac.za (E.M.N. Chirwa).

https://doi.org/10.1016/j.jphotochem.2024.116252
Received 25 July 2024; Received in revised form 18 December 2024; Accepted 29 December 2024
Available online 3 January 2025

plants (WWTPs) are not designed to remove pharmaceutical compounds and are unable to degrade these organic contaminants [8]. Physico-chemical technologies have been applied in the removal of antibiotics and it has been noted that the removal of these compounds using these technologies is expensive, requires high-energy input and sometimes inefficient and generates toxic sludge [9]. Chemical processes such as advanced oxidation processes (AOPs) have been identified as viable methods for the degradation and mineralization of organic pollutants in wastewater by utilizing highly reactive and oxidizing radicals. Heterogenous semiconductor photocatalysis, an AOP has emerged as an effective, eco-friendly, cost and energy efficient technique for the removal of these antibiotics from wastewater [10].

Semiconductor photocatalysis involves the use of semiconductors that are activated by sufficient light irradiation to generate electrons and holes. These electrons and holes initiate the oxidation of organic molecules by producing reactive radicals like (•OH) and ($\bullet O_2^-$). These radical species are strong oxidizers that make them effective for the degradation of diverse organic pollutants [11]. Visible-light-responsive photocatalysts are preferred because of their capacity to harness solar energy to make photocatalysis a green technology. Elmolla and Chaudhuri [12] study revealed that traditional ZnO semiconductor serves as a low cost and environmentally friendly photocatalyst for the degradation of antibiotics when exposed to UV light due to its suitable band gap. However, it can suffer from poor visible-light absorption owing to its wide band gap. Various Ag-semiconductor photocatalysts, such as Ag_2O and AgX (X = Cl, Br, I), show promise as visible-light-driven photocatalysts because of their strong reactivity; however, they often experience chemical stability issues due to photochemical corrosion [13]. Therefore, the exploration of innovative, cost-effective, non-toxic, and stable photocatalysts that can be activated by visible light irradiation has become key in photocatalysis.

Graphitic carbon nitride (g-C_3N_4), a fascinating metal-free semiconductor, is a promising semiconductor owing to its appealing properties such as a moderate band gap to respond to visible light, high chemical stability, exceptional electronic structure, and simple and eco-friendly synthesis [14]. However, the photocatalytic activity of pristine g-C_3N_4 has drawbacks, such as fast recombination of photo-induced charge carriers and low visible light utilization [15]. Various strategies have been explored to overcome these shortcomings, such as catalyst morphology control, element doping, and constructing heterojunctions to improve photocatalytic activity [16]. Tuning the morphology and internal structure of g-C_3N_4 is presumed to have a determining effect on the optical and photoelectronic properties [17]. g-C_3N_4 nanosheets have been reported to exhibit distinct physical and chemical structures with large specific areas and outstanding electronic mobility. This structure provides a larger surface area, shorter transfer length of photoinduced charge carriers, and enhanced light absorption, which improves the photocatalytic performance of g-C_3N_4 in the degradation of organic pollutants [18]. Porous hierarchical g-C_3N_4 has been reported to enhance catalyst light absorption and suppress charge recombination, thereby improving photocatalytic activity [19]. Porous g-C_3N_4 materials are commonly synthesised via hard or soft templating. However, both this approaches present challenges such as complexity of the process, structural defects and environmental pollution [20]. As a result, there is a need for development of efficient and eco-friendly methods to synthesis porous g-C_3N_4 materials.

In recent years, numerous studies have developed porous g-C_3N_4 photocatalysts with varying morphologies and modifications to enhance their photocatalytic activity. However, many of these designs still face limitations, such as rapid recombination of photogenerated electron-hole pairs, limited light absorption, or challenges in scalability and reproducibility. Our study introduces a novel porous g-C_3N_4 nanosheet structure synthesized via a streamlined, eco-friendly process that improves surface area, optimizes pore distribution, and tunes the band gap for efficient visible-light absorption. This structure not only enhances charge separation but also increases the number of reactive sites, making it highly effective for degrading tetracycline (TC). Compared to traditional bulk or non-porous g-C_3N_4 catalysts, our porous nanosheets demonstrate superior recyclability and stability across multiple degradation cycles, showcasing significant potential for scalable water treatment applications. The synthesized material was characterized to evaluate its physicochemical and optical properties. The photocatalytic efficiency of the material was investigated for the degradation of tetracycline. A possible photodegradation mechanism is proposed based on scavenger trapping experiments.

2. Material and methods

2.1. Chemicals and reagents

Melamine powder ($C_3H_6N_6$), ammonium bicarbonate (NH_4HCO_3). These chemicals were used as precursors for the synthesis of g-C_3N_4 materials, bulk, nanosheets and porous nanosheets. HPLC grade tetracycline ($C_{22}H_{24}N_2O_8{\cdot}xH_2O$) and HPLC grade methanol (≥99.9 %) (CH_3OH). Sodium hydroxide (NaOH) and hydrochloric acid (HCl) were used for pH adjustments. Radical scavenger tests were conducted using p-benzoquinone (BQ), 2-Propanol (IPA), ethylenediaminetetraacetic acid (EDTA) and hydrogen peroxide (H_2O_2). All chemicals and reagents were purchased from Sigma Aldrich and were used without further purification. Deionised water produced by an Elga Purelab Chorus unit purifier.

2.2. Catalyst synthesis

The three g-C_3N_4 photocatalysts were synthesized through thermal polymerization and pyrocondensation polymerization method. For bulk g-C_3N_4, 10 g of melamine powder was added to an alumina crucible with cover and heated at 600 °C for 4 h, followed by milling, washing with ethanol and deionized water, and dying at 80 °C overnight. The resulting product was named B-CN. g-C_3N_4 nanosheets were prepared by a similar method for bulk g-C_3N_4 but with a 2-hours heating followed by milling and a subsequent reheat at 600 °C for 2 h to obtain nanosheets, product was named CNN. Porous g-C_3N_4 nanosheets were synthesized by dissolving 10 g of each of melamine and ammonium bicarbonate in deionized water, followed by drying the mixture at 95 °C for approximately 24 h. The resulting material was subjected to the same heating, milling and washing procedure used to prepare g-C_3N_4 nanosheets, it was then named as P-CNN, method adopted and modified from Liu et al. [21].

2.3. Characterization

The X-ray diffraction (XRD) spectra of the prepared samples were analysed using a PANalytical X'Pert Pro powder diffractometer in θ–θ configuration with an X'Celerator detector and variable divergence- and fixed receiving slits with Fe filtered Co-Kα radiation (λ = 1.789 Å). The mineralogy was determined by selecting the best–fitting pattern from the ICSD database to the measured diffraction pattern, using X'Pert Highscore plus software. A PerkinElmer ATR 4000 Fourier-transform infrared (FTIR) spectrophotometer was used determine the chemical and functional group present in the synthesised photocatalysts. The spectra scan of the samples was detected within a wavelength from 4000 cm^{-1} to 600 cm^{-1} with a resolution of 4 cm^{-1} and 16 scans. A Zeiss Ultra PLUS FEG SEM using the Oxford instruments detector and AZtec 3.0 software SP1 was used to analyse and capture the images of the particle's morphology. A JOEL JEM 2100F, 200 kV analytical electron microscope was used to capture high resolution TEM images of the nanoparticles. The specific surface area and porosity of the materials was determined using a St 1 on NOVA touch 2LX BET system. The samples were degassed overnight with pure nitrogen flow at 27 °C to remove all the water molecules prior to the analysis of their surface areas and pore sizes. The conditions for analysis were N_2 analysis

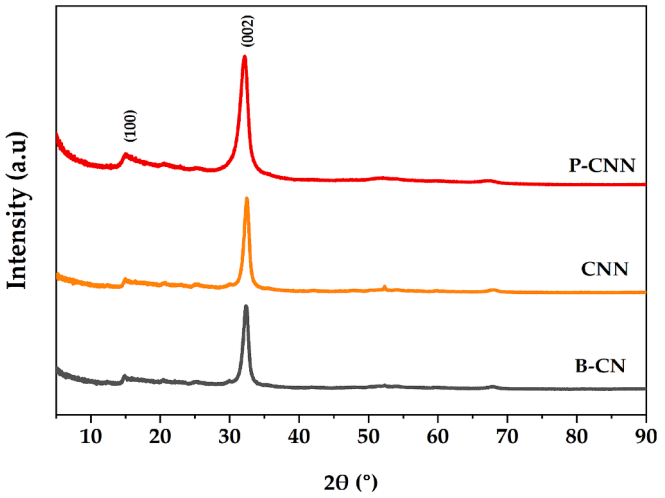

Fig. 1. XRD pattern of bulk g-C_3N_4 (B-CN), g-C_3N_4 nanosheets (CNN) and porous g-C_3N_4 nanosheets (P-CNN).

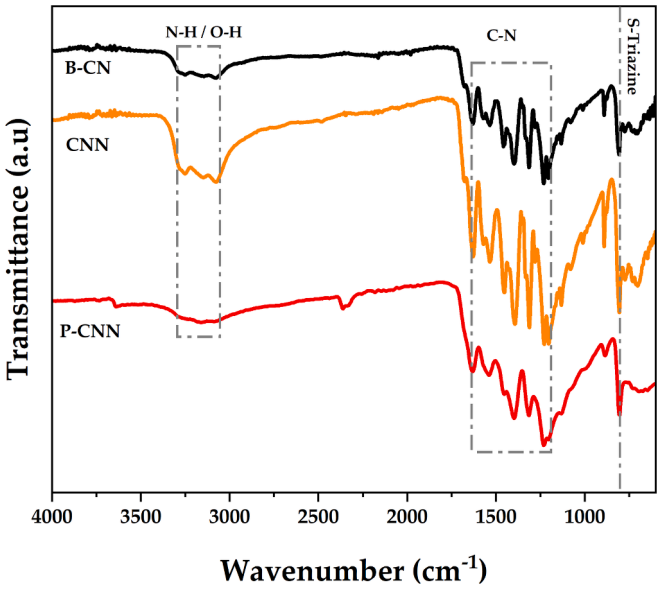

Fig. 2. FTIR spectra of all the synthesized g-C_3N_4 photocatalysts.

adsorptive, with liquid nitrogen bath temperature of 77.35 K at 5 secs equilibration interval. The standard multi-point BET measurements were followed. The optical absorption spectra of the synthesised particles were determined with a UV–Visible spectrophotometer Hitachi U-3900 double-beam single-monochromatic system with a UV-solutions software program.

2.4. Photocatalytic activity

The photocatalytic efficiency of the synthesised materials was determined by degrading tetracycline under visible light irradiation. Tetracycline stock solution of 100 mg/L concentration was prepared by dissolving 0.1 g of TC in 5 mL of methanol before being topped with deionised water to the 1 L mark, thereafter dilutions were prepared from these stock solutions to make desired concentrations. The photocatalytic tests were carried out at room temperature using a sealed batch photochemical reactor (Lelesil Innovative systems) with the capacity of 1 L, equipped with a 450 W visible lamp. The typical test solutions consisted of 500 mL of TC solution, 0.5 g of the synthesised photocatalyst and a magnetic stirrer to ensure a homogeneous dispersion of the pollutant and catalyst. The test solution was stirred in the dark for 30 min to reach adsorption/desorption equilibrium. Thereafter, the suspension was irradiated, and a 5 mL of aliquots samples were collected at certain time interval. These aliquots were centrifuged and filtered through 0.45 μm simplepure filters for the removal of photocatalyst before analysis. Optimization studies to determine the optimum degradation conditions were carried out by varying the catalyst loading and initial concentration. The concentration of tetracycline and progressive degradation was measured using a Jenway 7205 UV/Visible spectrophotometer at a wavelength of 357 nm. The total degradation of tetracycline after 2 h was evaluated using the expression shown in Eq. (1).

$$\%Degradation = \frac{C_0 - C_t}{C_0} \times 100 \quad (1)$$

where C_0 is the initial tetracycline concentration and C_t is the concentration of tetracycline at any given time, t.

Additionally, scavenger tests were performed to determine the dominant reacting species. These were conducted by adding 10 mmol of p-benzoquinone (BQ for $\bullet O_2^-$ radicals), 2-propanol (IPA for $\bullet$OH radicals), ethylenediaminetetraacetic acid (EDTA for h^+ VB) and hydrogen peroxide (h_2O_2 for e^- CB) separately to the reaction mixture while keeping constant the concentration at 10 ppm and 1 g/L catalyst loading, at room temperature. The recyclability and stability potential of porous g-C_3N_4 nanosheets was investigated for 5 cycles. After each cycle, a sample was taken, and the remaining solution was centrifuged and decanted. The catalyst recovered was dried at 80 °C for 12 h before being re-used in a fresh TC solution for another run.

3. Results and discussion

3.1. Material characterization

3.1.1. XRD analysis

The X-ray diffraction patterns were collected to examine the phases and crystal structures of the self-tuned g-C_3N_4 synthesized to form different morphology/intrinsic structure (bulk, ultrathin nanosheets and porous ultrathin nanosheets). As shown in Fig. 1, the XRD patterns of the samples are analogous to bulk g-C_3N_4. The appearance of well-defined and recognizable diffraction peaks at about 15° and 32° were perfectly indexed to the hexagonal phase of g-C_3N_4 and following miller indices (1 0 0) and (0 0 2) are coordinated well with the model data (JCPDS 87-1526) [22]. The relatively intense and sharp interlayer-stacking peak (0 0 2) at 32° indicates that a graphitic structure was formed and suggests a high degree of crystallinity in the materials. In addition, the minor crystal peak (1 0 0) at 15° relates to the in-plane structuring packing of nitrogen-linked heptazine unit [23]. The peaks on plane (0 0 2) were revealed to increase the intensity in the order of B-CN < CNN < P-CNN, suggesting an enhancement in the crystallinity of the materials which can be attributed to the increase in the surface area of the materials [24]. No additional peaks for other impurities or phases were detected, this confirms purity of the as-prepared g-C_3N_4 samples and shows that ammonium bicarbonate has no effect on the formation of g-C_3N_4 and alteration of its lattice structure.

3.1.2. FTIR spectroscopy analysis

The chemical structure of the synthesised material was examined using FTIR to investigate the effect of the modifying agents on the functional groups present in the materials. As depicted in Fig. 2, the spectra display three identical distinctive absorption bands corresponding to a typical g-C_3N_4 in all the photocatalysts: bulk g-C_3N_4, g-C_3N_4 nanosheets and porous g-C_3N_4 nanosheets, demonstrating comparable chemical features and retention of fundamental surface functional units even after addition of pore forming NH_4HCO_3. The broad absorption band at 3000–3200 cm^{-1} was ascribed to N—H bond of the uncondensed amino group and O—H vibration from surface-bound water. A strong band observed from 1200 to 1650 cm^{-1}

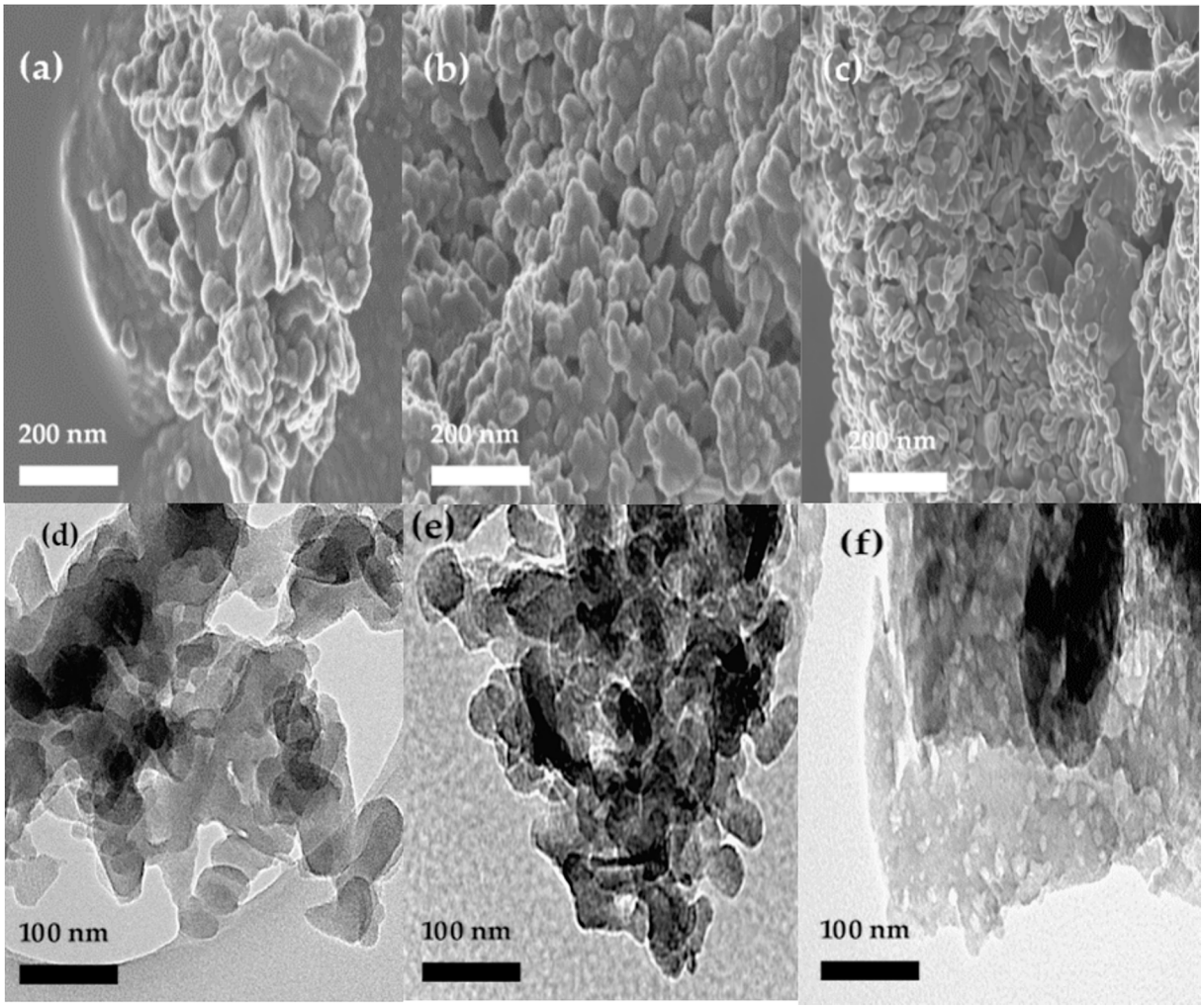

Fig. 3. SEM images of (a) B-CN, (b) CNN, (c) P-CNN and TEM images of (d) B-CN, (e) CNN, (f) P-CNN.

corresponding to heptazine ring stretching vibrations associated with the aromatic CN heterocycles presented an out-of-planar structure. The peak at 800 cm^{-1} was attributed to the s-triazine ring vibrations from the condensed carbon and nitrogen heterocycles exhibiting a planar structure [25]. A distinctive peak around 2300 cm^{-1}, corresponding to carbon dioxide was observed on P-CNN [26].

3.1.3. Catalyst morphology and microstructure

The morphology and microstructure of the three different g-C_3N_4 (bulk, nanosheets and porous nanosheets) photocatalysts was analysed by SEM and TEM to study the role of NH_4HCO_3 and the second annealing treatment, the captured images are presented in Fig. 3 (a)–(f). Bulk g-C_3N_4 unveiled lamellar and bulky irregular stacked sheets with thick structure predominately on its edges ((a) and (d)), this agglomeration is primarily caused by high temperature thermal polymerization during catalyst synthesis. Remarkably, the grinding and second annealing treatment was significant in modifying the bulky structure as shown in (b) and (e) CNN exhibited more dispersed and thinner stacked sheets, sheet size was shrivelled and maintained the lamellar structure. In contrast, the fine-tuned g-C_3N_4 (PCN) revealed a hierarchical porous structure while retaining the ultrathin layering, size, and dispersion of the nanosheets (c) and (f)) as anticipated. The formation of pores was due to the ongoing release of NH_3 and CO_2 gases from NH_4HCO_3 during pyrocondensation [27]. Certainly, the released gases had a notable role in the thermal polymerization at high temperature by improving heat transfer during reaction and acted as a template for bubbles thereby enabling the fabrication of a decentralized porous layered structure.

Table 1
Surface area and pore size distribution.

g-C_3N_4 material	Surface area (m^2/g)	Total Pore Volume (cm^3/g)	Average particle diameter (nm)
Bulk (B-CN)	13.28	3.87	2.05
Nanosheets (CNN)	38.39	7.90	7.10
Porous nanosheets (P-CNN)	47.47	8.96	5.75

3.1.4. Surface area and pore size analysis

The Brunauer-Emmett-Teller specific surface area and porosity of the three samples was determined by using Nitrogen adsorption–desorption measurements and the results are summarized in Table 1. Compared to BCN (surface area = 13.28 m^2/g, total pore volume = 3.87 cm^3/g) and CNN (surface area = 38.39 m^2/g, total pore volume = 7.90 cm^3/g), PCN (surface area = 47.47 m^2/g, total pore volume = 8.96 cm^3/g) revealed a higher surface area and pore volume. These results were consistent with the SEM and TEM images inserts in Fig. 3, signifying that surface defects on g-C_3N_4 material facilitated the enhancement of surface area. Increase in pore volume and surface area is deemed beneficial for efficient photocatalytic degradation of pollutants by boosting optical adsorption capacity of the material and offers more reactive sites for effective degradation of pollutants [28,29].

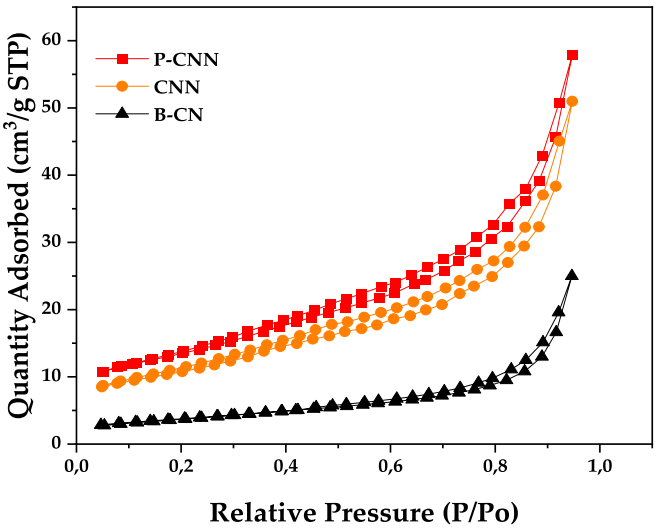

Fig. 4. N_2 adsorption–desorption isotherms of all the synthesized photocatalysts.

The N_2 adsorption–desorption isotherms measurements were conducted for the as-synthesised g-C_3N_4 materials, BCN, CNN and PCN. The results are depicted in Fig. 4, the isotherm patterns of all the samples exhibited characteristics of Type IV isotherm according to the International Union of Pure and Applied Chemistry (IUPAC) classification [30]. Notably, the hysteresis loop of PCN and CNN took on an H3 type shape in the relative pressure range of 0.7–0.9, suggesting that the material consist of mesoporous structure, and this further agrees with the porosity/textural properties of the materials. BCN displayed a lower N_2 absorption probably due to lack of porosity, and a remarkable increase was observed between CNN and PCN.

3.1.5. *Photo-absorption and band gap analysis*

The effect of morphology on the optical properties of the as-prepared g-C_3N_4 samples was studied by conducting a UV–vis diffuse reflectance spectroscopy (DRS) analysis. As depicted in Fig. 5 (a) the light absorption of all the samples effectively increased in the visible region when compared to B-CN. The light absorption edge of CNN and P-CNN exhibited a slight red shift compared to B-CN, with band edge positions at 400 nm for B-CN, 403 nm for CNN and 407 nm for P-CNN. The redshift can be ascribed to the smaller particles size and porous morphology of the catalysts, which expands the optical absorbance range of the materials. This confirms that changes on morphology influence the optical absorption of g-C_3N_4. The corresponding band gap energies were determined by Tauc model as defined by Eq. (2).

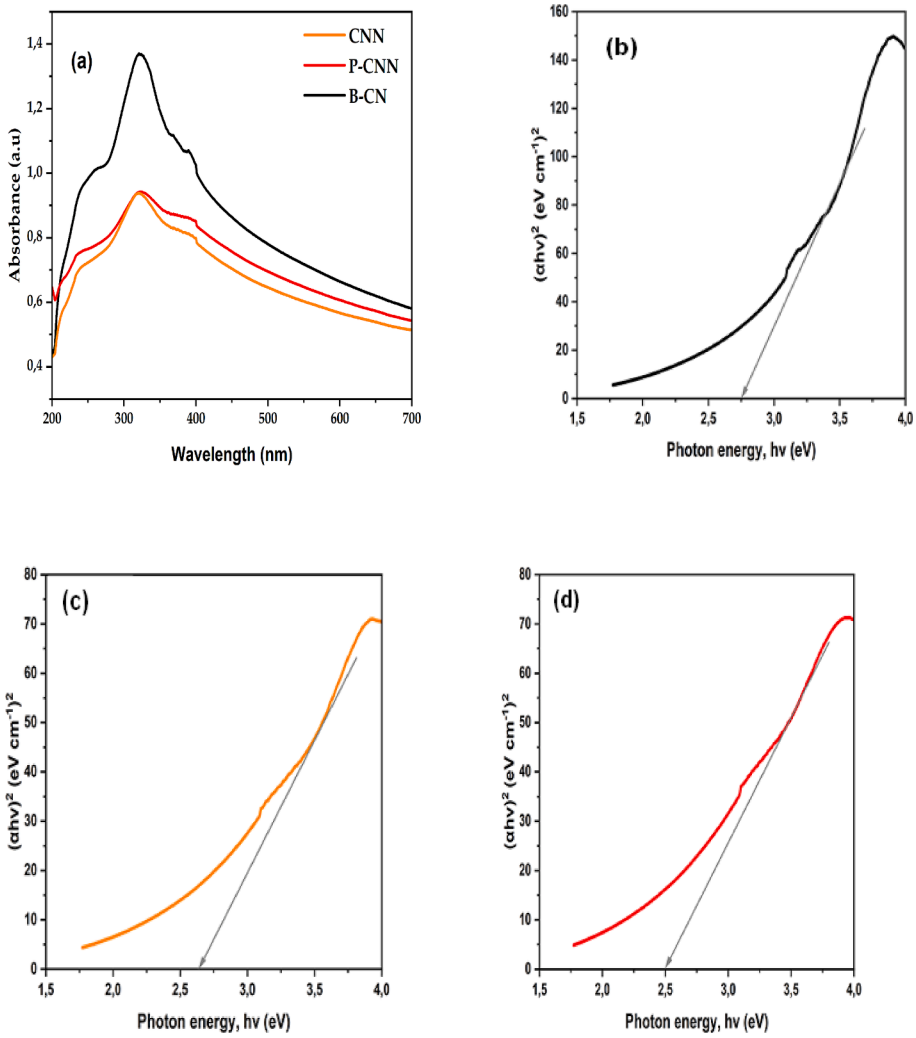

Fig. 5. (a) UV–vis absorption spectra of synthesized g-C_3N_4 materials. Tauc plot and estimated band gap for (b) Bulk g-C_3N_4, (c) g-C_3N_4 nanosheets and (d) porous g-C_3N_4 nanosheets.

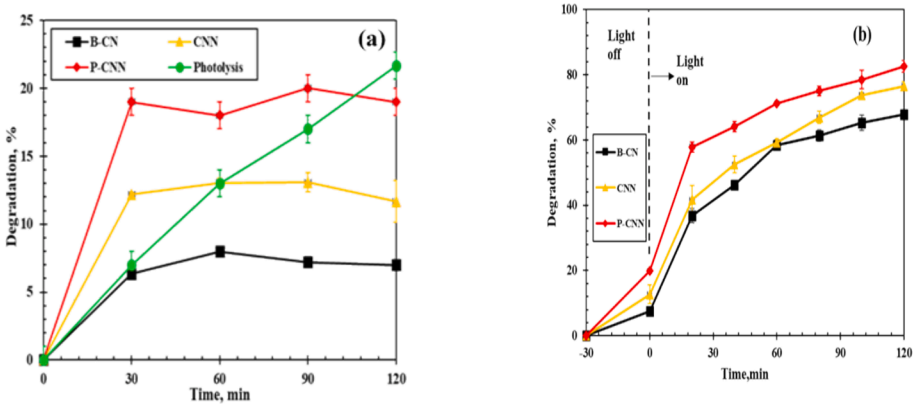

Fig. 6. Photocatalytic performance of each g-C_3N_4 photocatalyst, (a) Controlled experiment and (b) degradation experiment under visible light irradiation.

$$(\alpha h\nu)^n = A(h\nu - E_g) \quad (2)$$

where α is the absorption coefficient, h is Planck's constant, v is the photon's frequency, A is a proportionality constant,E_g is the band gap energy and n denote the nature of the electron transition, where n is assumed to be 2 or 1/2 for direct and indirect transition, respectively.

The band gap energy for each sample was estimated by pinpointing the horizontal axis intercept of tangents drawn on the plots of $(\alpha h\nu)^2$ against band energy, since they all displayed direct band gaps. The optical band gap energy of B-CN, CNN and P-CNN were estimated to be 2.75 eV, 2.63 eV and 2.50 eV, respectively as presented in Fig. 5 (b), (c) and (d). Implying that there is a significant alteration in the electronic structure of g-C_3N_4. After the second annealing, the band gap of B-CN was narrowed from 2.75 eV to 2.63 eV for CNN. A previous study by Yang et al. [31] had also noted band gap energy reduction by a similar factor to the one observed in this study, with 2.5 eV for bulk g-C_3N_4 and 2.4 eV for g-C_3N_4 nanosheets. The incorporation of the hierarchical porous structure and the 2D layering of the g-C_3N_4 further narrowed the band gap energy to 2.50 eV. The reduction of the band gap serves not only to decrease the energy necessary for electron transition between the conduction and valence bands but also to enhance absorption of visible light [32]. This results to an increase generation of photogenerated carriers because of the 2D layering, and improved separation of photogenerated charge carriers achieved through multiple reflections facilitated by the porous structure of g-C_3N_4 [33]. Consequently, an improved photocatalytic performance can be anticipated.

3.2. Photocatalytic degradation activity

3.2.1. Effect of catalyst morphology

The photocatalytic performance of the as-prepared B-CN, CNN and P-CNN photocatalysts was evaluated using 10 ppm tetracycline solution under visible light irradiation and 1 gL^{-1} catalyst loading. The solution was stirred in the dark for 30 min until adsorption–desorption equilibrium was reached and then the solution was irradiated for 120 min. Control experiments were conducted to elucidate the individual contributions of photolysis and adsorption to tetracycline degradation. As presented in Fig. 6, The removal of TC in photolysis control experiments resulted in 22 % degradation, indicating that TC has a low susceptibility to degradation by light alone. For Adsorption experiments, 19 % of TC was adsorbed on P-CNN after 2 h while 12 % TC was adsorbed on CNN and 9 % was adsorbed on B-CN, these results can be associated with the surface area of the materials and adsorption–desorption equilibrium of TC to the surface of the catalysts in the dark. Fig. 6 (a) present the degradation efficiency of the as-prepared B-CN, CNN and P-CNN. After visible light irradiation, the photodegradation efficiency of TC was 68 % with B-CN whereas CNN exhibited 77 % and higher degradation of 83 % was observed with P-CNN. Compared to B-CN and CNN, the degradation

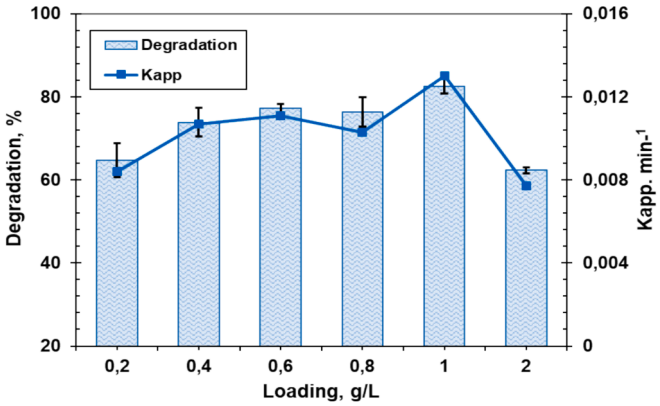

Fig. 7. Effect of catalyst loading on photocatalytic degradation of Tetracycline and the rate constant, 10 ppm tetracycline concentration.

efficiency of P-CNN was significantly improved. These results align with the BET, Photo-absorption and band gap analysis results. The improved photocatalytic performance can be attributed to the dual effect of porous and nanosheets morphology resulting in an increased surface area, which offers an abundance of active sites for reactions, heightened light absorption leading to more efficient reaction, and enhanced charge separation that minimizes electron-hole re-combination, an essential factor for efficient photocatalysis. In a study by Hao et al. [34] it was observed that the degradation of TC (10 ppm) reached 58.07 % with bulk g-C_3N_4 and 72.01 % with porous g-C_3N_4 nanosheets after 120 min of visible light irradiation. These degradation rates were found to be lower compared to those achieved with the as-synthesized B-CN and P-CNN materials in this study. Notably, the photoactivity phenomenon is consistent in both studies. The variation in degradation rates could potentially be ascribed to the different synthetic methods used in preparing the catalysts, which in turn influence the catalysts textural and optical properties [35].

3.2.2. Effect of catalyst loading

Numerous studies reported the existence of optimal catalyst dosage for effective photodegradation of organic contaminants and indicated that the specific optimal dosage is influenced by nature of the photocatalyst [36]. To test the influence of catalyst loading on the degradation of TC, different masses of porous g-C_3N_4 nanosheets were loaded in TC solution (10 ppm). As demonstrated in Fig. 7, the degradation efficiency of TC increased with increasing catalyst concentration from 0.2 to 1 g/L by degradation of 65 %–83 %. However, a decrease in degradation efficiency by 21 % was observed at 2 g/L. The increase in the efficiency can be attributed to enhanced light absorption and the increase of the

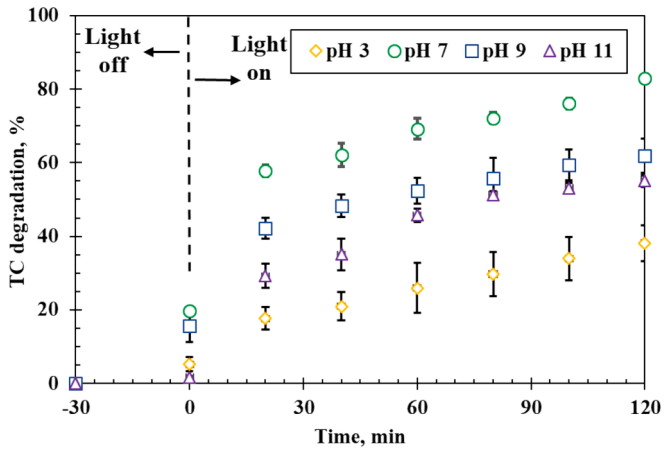

Fig. 8. Effect of initial pH on tetracycline photodegradation.

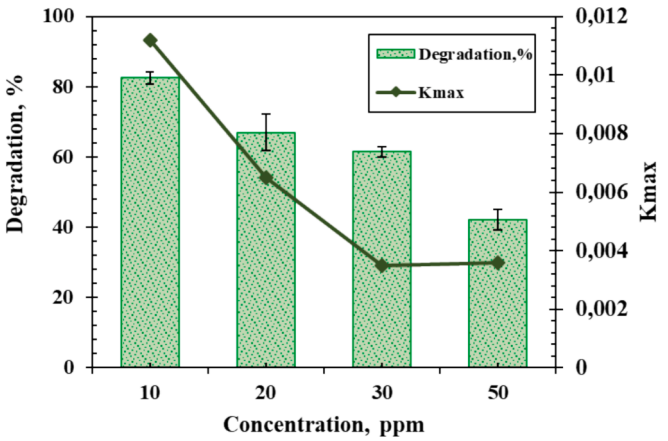

Fig. 9. Effect of initial concentration and kinetics on photocatalytic degradation of TC, at 1 gL-1 catalyst loading.

number of active sites on the catalyst surface which eventually cause the generation of more reactive species ($\bullet O_2^-$, •OH) that will participate in the degradation of TC as a result of the increasing catalyst loading [37]. The decrease in degradation efficiency at 2 g/L loading can be ascribed to turbidity and agglomeration because of the increased catalyst dosage [38]. The turbidity increases with the increasing quantity of photocatalyst, and subsequently lead to light scattering, caused by the collision of optical rays with the scattered catalyst particles in the solution. As a result, numerous light photons lose their energy resulting to a decreased efficiency of photocatalytic degradation performance. On the other hand, agglomeration can be due particle size. Based on the results, the optimum catalyst concentration for the degradation of tetracycline in an aqueous solution was found to be 1 g/L.

The degradation kinetics at different catalyst loading were analysed, using the Langmuir-Hinshelwood kinetics model expressed in equation (3).

$$\ln\left(\frac{C_0}{C_t}\right) = K_{app}t \tag{3}$$

where C_0 *and* C_t represents the concentration of TC before degradation and at different times during photodegradation respectively. K_{app} is the pseudo-first-order rate constant.

The rate constant of a photocatalytic reaction is closely influenced by the structural characteristics of the catalyst, including surface area, pore size and morphology. The rate constants as shown in Fig. 7 revealed a parallel pattern with the degradation. A steady increase in the K_{app} was apparent as the catalyst loading increased. The rate constant showed an increase, elevating from 0.0084 min^{-1} at loading of 0.2 gL^{-1} to 0.013 min^{-1} at 1 gL^{-1}. This can be ascribed to the catalyst's surface area, whereby increasing the catalyst concentration increases its surface area, providing more active sites for tetracycline to adsorb and react, which enhances the rate reaction and results in higher rate constant. However, the hypothesized combined effect of turbidity and particle agglomeration decreased the catalyst's effective surface area and led to a notable decline, reducing the rate constant to 0.0077 min^{-1} when the catalyst loading was doubled to 2 gL^{-1} [39]. Remarkably, the Langmuir-Hinshelwood kinetic model provided the best fit for the results at 2 gL^{-1} boasting a high R^2 value of 0.97, and 1 gL^{-1}, 0.8 gL^{-1} and 0.4 gL^{-1} yielded R^2 value at 0.93, 0.91 and 0.91 respectively.

3.2.3. *Effect of initial pH*

The initial pH of a solution plays a crucial role in photocatalytic processes by affecting the stability and surface charge of the catalyst and the target organic compound speciation. The speciation of TC molecules exists as positively charged TCH_3^+ at pH below 3.3, as neutral zwitterions TCH_2^0 between pH 3.3 and 7.7, as negatively charged TCH^- ions between pH 7.7 and 9.0 and as negative charged TC^{2-} at pH above 9.0 [40]. The surface charge of g-C_3N_4 synthesised from melamine exhibit a pH dependent behaviour. At pH values below 5, the particles are positive due to protonated amino group. Conversely, above pH value of 5, the surface is negatively charged as amino group lose a proton [41]. The effect of pH on tetracycline photodegradation by porous g-C_3N_4 nanosheets was explored in the pH range of 3–11. As illustrated in Fig. 8, the degradation efficiency of TC increased from 38 % to 83 % with the increase of pH from 3 to 7, then decreased to 62 % and 55 % with further increase of pH to 9 and 11. The optimum pH for porous g-C_3N_4 nanosheets photocatalytic degradation of TC was obtained at a pH of 7. The observed variations in degradation efficiency at different pH levels can be explained by interplay of charge interaction between the surface of P-CNN and TC molecules. As the pH increases from 3 to 7, TC undergoes a transition from positively charged to neutral, while the surface of P-CNN changes from positive to negative. This shift in charges may result in electrostatic attraction that enhances TC adsorption onto P-CNN and facilitates further degradation. However, as the pH further increases from 7 to 11, TC becomes negatively charged and P-CNN remain negative. Consequently, the resulting electrostatic repulsion weakens the adsorption capacity, leading to a decrease in photodegradation efficiency. The findings from this study aligns with previous observation in the photocatalytic degradation of tetracycline [42,43].

3.2.4. *Effect of initial TC concentration*

To investigate the effect of initial TC concentrations on the photocatalytic degradation of TC, varying concentrations of 10, 20, 30 and 50 ppm were studied. This was done under optimum condition (1) g/L catalyst loading and a pH of 7. As depicted in Fig. 9, the removal efficiency decreased from 83 % to 42 % with the increasing TC concentrations from 10 ppm to 50 ppm. A similar trend was reported by Huo et al. [44] It is presumed that during the photodegradation the active sites of the catalyst and the photogenerated species formed on the surface of the catalyst were constant throughout the experiments. Increased TC concentration cause adsorption of excess TC molecules onto the catalyst surface thereby saturates the active sites and reduce the generation of active species ($\bullet O_2^-$ and •OH) necessary for the photodegradation reaction, which subsequently decrease the removal efficiency due to insufficient reactants. Additionally, this can be rationalized on the basis that TC is a coloured compound in solution and this colour increases in intensity with concentration. Therefore, with increasing concentrations of TC, the solution becomes highly saturated with TC ions thereby diminish light penetration. Accordingly, a significant fraction of emitted photons is absorbed by the solution which consequently lowers photon adsorption to initiate electron hole separation on the catalyst particles and results to low photocatalytic

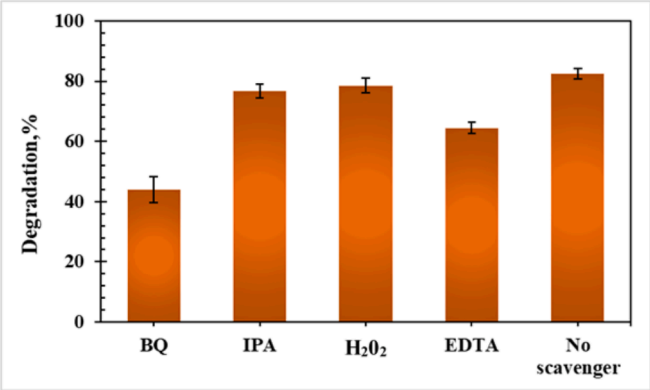

Fig. 10. Effect of different scavengers on Tetracycline degradation with porous g-C_3N_4 photocatalyst.

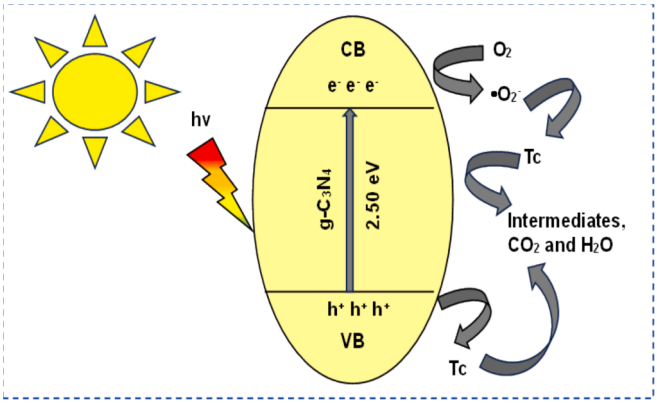

Fig. 11. Proposed degradation mechanism of porous g-C_3N_4 nanosheets in the photocatalytic degradation of Tetracycline.

efficiency. Chen et al. [45] explained that the gradual decrease in TC removal efficiency with increasing concentrations can also be due to the competition of the as-generated intermediates with the parent TC molecules for limited adsorption and interaction with radical species on the catalyst surface at high TC concentration, this deteriorates the photodegradation efficiency. The optimum concentration of TC was 10 ppm in these experimental conditions. The most significant degradation rate was observed when the initial concentration was 10 ppm. The rate constants exhibited decreasing trend with the increasing concentration. In specific, 10 ppm solution had a constant rate of 0.0112 min^{-1} in contrast to 50 ppm solution which displayed a lower constant rate of 0.0036 min^{-1}. At low initial pollutant concentration, the reaction rate increase because there are sufficient active sites for efficient interaction. However, with increasing pollutant concentration, the surface area becomes limited, saturating active sites and increasing activation energy, resulting to a decline in reaction rate and lower rate constant [46].

3.2.5. Radical scavenging test

It is widely recognized that radical species are crucial determinants for photodegradation reactions. Herein, quenching experiments were performed to probe the role of reactive species in the photocatalytic degradation of TC using the synthesised catalyst. For this purpose, 10 mmol of p-Benzoquinone (BQ) as a superoxide ($\bullet O_2^-$) radical scavenger, 2-propanol (IPA) as a hydroxyl radical ($\bullet OH$) scavenger, Hydrogen peroxide (H_2O_2) as an electron (e^-) scavenger and ethylenediaminetetraacetic acid (EDTA) as a hole (h^+) scavenger were added separately to the reaction mixture while keep constant the concentration of 10 ppm and 1 g/L catalyst loading. Fig. 10, reveals the effects of the different scavengers and no scavenger on photodegradation of TC. The incorporation of BQ drastically suppressed the degradation process as compared to the other scavenger reactions with a removal efficiency of 44 %, this suggests that superoxide radicals were the major reactive species for degradation of TC. However, the addition of IPA and H_2O_2 had an insignificant effect on the photodegradation efficiency with removal efficiency of 77 % and 78 % respectively, and the addition of EDTA had a noticeable quenching effect with 64 % removal efficiency. According to these results, it can be deduced that superoxide radical and the species generated via hole carriers are the most reactive species involved in the degradation of tetracycline.

3.2.6. Proposed mechanism

Based on the radical scavenging experiments, a schematic of the possible mechanism for the photocatalytic degradation of tetracycline by porous g-C_3N_4 nanosheets (PCNN) under visible light irradiation is proposed in Fig. 11. In photocatalysis, effective separation of electron and hole pairs is widely recognized as a crucial factor for ensuring a high reactivity of photocatalysts [47]. Bulk g-C_3N_4 photocatalytic activity is restricted by fast recombination of the photogenerated e^- & h^+ which consequently affects the efficient degradation of the pollutants. As verified by the UV–vis reflectance spectra, the band gap of PCNNs was reduced to 2.50 eV. The tuned band gap is due the structural modification (porous and 2D nanosheets) of g-C_3N_4 which improve the photocatalytic activity of the material by enhancing the materials optical properties such as light absorption and promoting charge separation. The photocatalytic reaction begins with light exposure and absorption of photons with sufficient energy by porous g-C_3N_4 nanosheets. When the photons are absorbed by the PCNN, they excite electrons (e^-) within the valence band (VB), causing them to transition to the conduction band (CB), thus generating pairs of electron-hole (e^-/h^+) Eq. (4). The electrons (e^-) generated in the CB and holes (h^+) formed in the VB possess opposing charges and tend to move toward the surface of the photocatalyst. Subsequently, adsorbed oxygen from the system reacts with the electrons to form highly reactive superoxide radicals as confirmed by quenching experiments equation (5). These radicals, owing to their potent oxidative capacity, directly oxidized tetracycline equation (6). Moreover, the photogenerated holes (h^+) in the VB as powerful oxidants, directly initiate the oxidation of tetracycline adhering to the photocatalyst's surface equation (7). The combined oxidation action of photogenerated holes (h^+) and superoxide radicals ($\bullet O_2^-$) leads to the decomposition of tetracycline adhering to the photocatalyst's surface. This process can continue until the organic molecules are completely converted into harmless substances, such as CO_2, H_2O, and mineral ions. Panneri et al. [48] have also proposed a similar photocatalytic mechanism on the photocatalytic degradation of tetracycline using g-C_3N_4-Ag/ZnO as a catalyst.

$$g\text{-}C_3N_4 + hv \rightarrow g\text{-}C_3N_4\ (h_{VB}^+ + e_{CB}^-) \quad (4)$$

$$e_{CB}^- + O_2 \rightarrow \bullet O_2^- \quad (5)$$

$$\bullet O_2^- + TC \rightarrow (\text{intermediates}) \rightarrow CO_2 + H_2O \quad (6)$$

$$h_{VB}^+ + TC \rightarrow (\text{intermediates}) \rightarrow CO_2 + H_2O \quad (7)$$

To provide a further elucidation of the above mechanism, the conduction band (E_{CB}) and valence band (E_{VB}) potentials relative to normal hydrogen electrode (NHE) of the photocatalyst (P-CNN) were determine using the following equations:

$$E_{VB} = X - E^e + 0.5E_g \quad (8)$$

$$E_{CB} = E_{VB} - E_g \quad (9)$$

where X denotes the absolute electronegativity of the semiconductor. For g-C_3N_4, this value is 4.73 eV. E^e is the energy of free electrons on the hydrogen scale, which has a value of 4.5 eV and Eg is the bandgap energy.

The efficiency of interfacial charge transfer in heterogeneous

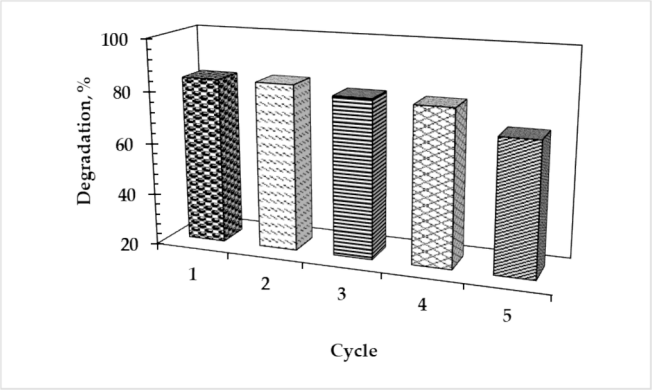

Fig. 12. Porous g-C_3N_4 nanosheets photocatalyst stability and recyclability for 5 cycles.

photocatalyst depends on the optimal alignment of the conduction and valence band energies within the photocatalyst. The valence band and conduction band potential of P-CNN were 1.48 eV and – 1,02 eV respectively. When exposure to visible light, g-C_3N_4 generates electrons in the conduction band and holes in the valence band. The conduction band of P-CNN (−1.02 eV vs. NHE) is more negative than the value of $O_2/\bullet O_2^-$ (0.33 eV vs. NHE), hence photogenerated electrons on the CB can react with oxygen molecules absorbed on the P-CNN surface, leading to their reduction into superoxide radicals ($\bullet O_2^-$). These superoxide radicals actively participate in the degradation of TC, resulting in the formation of CO_2 and H_2O. Conversely, the valence band (+1.48 eV vs. NHE) has a lower standard redox potential than that of H_20/OH (+2.38 eV vs NHE). This suggests that holes cannot oxide H_20 into OH radical species. However, they directly facilitate the degradation of TC.

3.2.7. *Catalyst recyclability*

The practical application of photocatalysts is significantly influenced by their recyclability and stability. To explore the recyclability and stability of the prepared porous g-C_3N_4 nanosheets for fresh TC degradation under same process conditions, five cyclic photocatalytic tests were conducted. Following each consecutive run, the catalyst particles were recovered by centrifugation followed by washing with ethanol and water before being dried at 80 °C for 12 h. The results as illustrated in Fig. 12, the catalyst exhibited a good stability after five cycle runs, with a slight decrease in degradation efficiency after four successive runs and a modest decrease at the fifth run by 16 % compared to first run. The decline in degradation efficiency can be attributed to the reduction of active sites, this reduction occurs as TC molecules and intermediates adsorb on the surface catalyst which then limits availability of active site to accommodate more of TC molecules and therefore decrease degradation efficiency [49]. The results reveal that the catalyst possess an excellent reusability and attests its practical application.

Fig. 13 displays XRD patterns and the FTIR spectra of P-CNN pre-treatment and after five cycles (post-treatment). The XRD patterns after the treatment exhibited two characteristics peaks similar to those observed before the initial treatment, specifically, peaks located at 15 and 32 corresponding to (100) and (002) miller indices. The peak intensity decreased following the five cycles and this can be ascribed to the agglomeration of catalyst particles. There is no significant change in the FTIR spectra of P-CNN before and after 5 cycles, the material retained its functional groups post treatment. Based on these results, it can be deduced that the synthesized P-CNN photocatalyst remains stable and can be utilized repeatedly for up to four cycles with no significant loss in its photocatalytic activity.

4. Conclusions

A facile one step method was utilized for the synthesis of g-C_3N_4 photocatalyst with distinct morphology including bulk, nanosheets and porous nanosheets. Characterization using diverse techniques confirmed the formation of the desired materials. Among these, porous g-C_3N_4 nanosheets exhibited a larger surface area and its band gap was reduced from 2.75 eV to 2.50 eV to compared to bulk g-C_3N_4. Notably, porous g-C_3N_4 showed an exceptional photocatalytic performance toward TC degradation compared to the other two catalysts. This enhanced performance was attributed to the abundant active sites, suppressed recombination and extended visible-light absorption. Radical scavenging experiments indicated that superoxide radicals and photogenerated holes were the dominant radical species responsible for TC removal in the P-CNN system. Furthermore, tests evaluating the photocatalytic stability and recyclability of porous g-C_3N_4 demonstrated that the photocatalyst can be reused for five consecutive cycles without undergoing significant phase changes. This study underlines a simple, feasible and green strategy of combining porous and 2D nanosheets structure on g-C_3N_4 for an enhanced and efficient visible-light-driven photocatalytic removal of antibiotics in an aqueous system, exemplified by TC.

Author contributions

Nothando Phakathi: conceptualization, methodology, Software, formal analysis, investigation, data curation, visualisation, writing-original draft. Shepherd Tichaphondwa: conceptualization, methodology, validation, resources, writing-review and editing, supervision, project administration. Evans Chirwa: conceptualization, resources, writing-review and editing, visualisation, supervision, funding acquisition.

CRediT authorship contribution statement

Nothando A. Phakathi: Conceptualization, Methodology, Software, Formal analysis, Investigation, Data curation, Visualization, Writing – original draft. **Shepherd M. Tichapondwa:** Writing – review & editing, Validation, Supervision, Resources, Project administration,

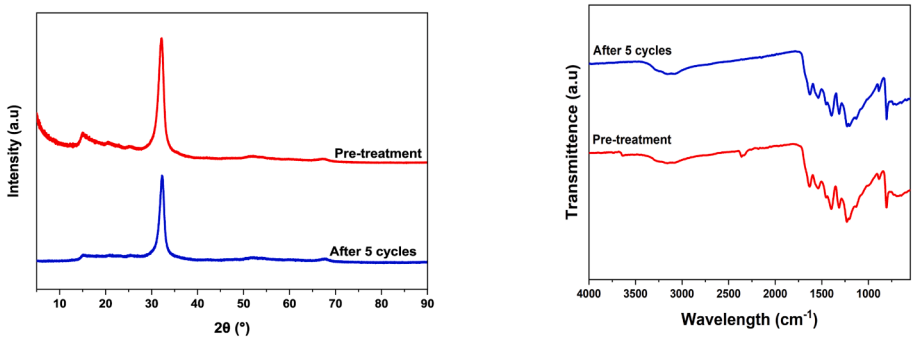

Fig. 13. XRD patterns and FTIR Spectra of porous g-C_3N_4 nanosheets pre-treatment and post-treatment.

Methodology, Conceptualization. **Evans M.N. Chirwa:** Conceptualization, Resources, Writing – review & editing, Visualization, Supervision, Funding acquisition.

Declaration of competing interest

The authors declare that they have no known competing financial interests or personal relationships that could have appeared to influence the work reported in this paper.

Acknowledgements

This research was funded by National Research Fund (NRF) of South Africa, grant number EQP180503325881 awarded to Prof Evans M. Nkhalambayausi Chirwa, The NRF Thuthuka Grant grant number TTK18024324064 awarded to Prof Shepherd Tichapondwa and Rand Water Chair in Water Utilisation, grant number RW01413/18.

Data availability

Data will be made available on request.

References

[1] H.E. Frech, R.D. Miller, The effects of pharmaceutical consumption and obesity on the quality of life in the Organization of Economic Cooperation and Development (OECD) countries, Pharmacoeconomics 22 (2004) 25–36, https://doi.org/10.2165/00019053-200422002-00004.
[2] G.-G. Ying, J.-L. Zhao, L.-J. Zhou, S. Liu, Chapter 14 - Fate and Occurrence of Pharmaceuticals in the Aquatic Environment (Surface Water and Sediment), Comprehens. Anal. Chem. 62 (2013) 453–557. https://doi.org/10.1016/B978-0-444-62657-8.00014-8.
[3] A. Gogoi, P. Mazumder, V.K. Tyagi, G.G. Tushara Chaminda, A.K. An, M. Kumar, Occurrence and fate of emerging contaminants in water environment: A review, Groundwater for, Sustain. Dev. 6 (2018) 169–180, https://doi.org/10.1016/j.gsd.2017.12.009.
[4] S. Fekadu, E. Alemayehu, R. Dewil, B. Van der Bruggen, Pharmaceuticals in freshwater aquatic environments: a comparison of the African and European challenge, Sci. Total Environ. 654 (2019) 324–337, https://doi.org/10.1016/j.scitotenv.2018.11.072.
[5] Y. Ben, C. Fu, M. Hu, L. Liu, M.H. Wong, C. Zheng, Human health risk assessment of antibiotic resistance associated with antibiotic residues in the environment: A review, 169 (2019) 483–493.
[6] M. Zhu, Y. Tang, X. Chen, B. Liao, Y. Yu, S. Hou, X. Fan, Internal electric field and oxygen vacancies synergistically optimized Ba2+ doped SrBi2B2O7 for photocatalytic tetracycline degradation from water, 433 (2022) 134580.
[7] R. Daghrir, P. Drogui, Tetracycline antibiotics in the environment: a review, 11 (2013) 209–227.
[8] T.A. Ternes, M. Meisenheimer, D. McDowell, F. Sacher, H.-J. Brauch, B. Haist-Gulde, G. Preuss, U. Wilme, N. Zulei-Seibert, Removal of pharmaceuticals during drinking water treatment, Environ. Sci. Technol. 36 (2002) 3855–3863, https://doi.org/10.1021/es015757k.
[9] B. Wang, H. Shi, M.Y. Habteselassie, X. Deng, Y. Teng, Y. Wang, Q. Huang, Simultaneous removal of multidrug-resistant Salmonella enterica serotype typhimurium, antibiotics and antibiotic resistance genes from water by electrooxidation on a Magnéli phase Ti4O7 anode, Chem. Eng. J. 407 (2021) 127134, https://doi.org/10.1016/j.cej.2020.127134.
[10] B. Lin, S. Li, Y. Peng, Z. Chen, X. Wang, MOF-derived core/shell C-TiO_2/$CoTiO_3$ type II heterojunction for efficient photocatalytic removal of antibiotics, J. Hazard. Mater. 406 (2021) 124675, https://doi.org/10.1016/j.jhazmat.2020.124675.
[11] Y. Li, F. Chen, R. He, Y. Wang, N. Tang, Chapter 24 - semiconductor photocatalysis for water purification, in: S. Thomas, D. Pasquini, S. Leu, D.A. Gopakumar (Eds.), Nanoscale Materials in Water Purification, Elsevier, 2019, pp. 689–705, https://doi.org/10.1016/B978-0-12-813926-4.00030-6.
[12] E.S. Elmolla, M. Chaudhuri, Degradation of amoxicillin, ampicillin and cloxacillin antibiotics in aqueous solution by the UV/ZnO photocatalytic process, J. Hazrd. Mater. 173 (2010) 445–449, https://doi.org/10.1016/j.jhazmat.2009.08.104.
[13] M. Moja, A. Mapossa, E. Chirwa, S. Tichapondwa, Photocatalytic degradation of 2,4–dichlorophenol using nanomaterials silver halide catalysts, Environ. Sci. Pollut. Res. 31 (2024) 16, https://doi.org/10.1007/s11356-024-31921-1.
[14] Q. Zheng, D.P. Durkin, J.E. Elenewski, Y. Sun, N.A. Banek, L. Hua, H. Chen, M. J. Wagner, W. Zhang, D. Shuai, Visible-light-responsive graphitic carbon nitride: rational design and photocatalytic applications for water treatment, Environ. Sci. Technol. 50 (2016) 12938–12948, https://doi.org/10.1021/acs.est.6b02579.
[15] W.-J. Ong, L.-L. Tan, Y.H. Ng, S.-T. Yong, S.-P. Chai, Graphitic carbon nitride (g-C3N4)-based photocatalysts for artificial photosynthesis and environmental remediation: are we a step closer to achieving sustainability? Chem. Rev. 116 (2016) 7159–7329, https://doi.org/10.1021/acs.chemrev.6b00075.
[16] J. Liang, X. Yang, Y. Wang, P. He, H. Fu, Y. Zhao, Q. Zou, X. An, A review on g-C3N4 incorporated with organics for enhanced photocatalytic water splitting, J. Mater. Chem. 9 (2021) 12898–12922, https://doi.org/10.1039/D1TA00890K.
[17] S. Patnaik, S. Martha, K.M. Parida, An overview of the structural, textural and morphological modulations of g-C_3N_4 towards photocatalytic hydrogen production, RSC Adv. 6 (2016) 46929–46951, https://doi.org/10.1039/C5RA26702A.
[18] H. He, L. Huang, Z. Zhong, S. Tan, Constructing three-dimensional porous graphene-carbon quantum dots/g-C_3N_4 nanosheet aerogel metal-free photocatalyst with enhanced photocatalytic activity, Appl. Surf. Sci. 441 (2018) 285–294, https://doi.org/10.1016/j.apsusc.2018.01.298.
[19] J. Fu, B. Zhu, C. Jiang, B. Cheng, W. You, J. Yu, Hierarchical porous O-doped g-C_3N_4 with enhanced photocatalytic CO_2 reduction activity, Small 13 (2017), https://doi.org/10.1002/smll.201603938.
[20] S. Obregón, A. Vázquez, M.A. Ruíz-Gómez, V. Rodríguez-González, SBA-15 assisted preparation of mesoporous g-C3N4 for photocatalytic H_2 production and Au^{3+} fluorescence sensing 488 (2019) 205–212. <https://doi.org/10.1016/j.apsusc.2019.05.231>.
[21] G. Liu, Z. Zhang, M. Lv, H. Wang, D. Chen, Y. Feng, Photodegradation performance and transformation mechanisms of sulfamethoxazole by porous g-C_3N_4 modified with ammonia bicarbonate, Sep. Purif. Technol. 235 (2019), https://doi.org/10.1016/j.seppur.2019.116172.
[22] H. Starukh, M. Koštejn, V. Matějka, P. Praus, Graphitic carbon nitride as a platform for the synthesis of silver nanoclusters, Nanoscale Res. Lett. 16 (2021) 166, https://doi.org/10.1186/s11671-021-03621-z.
[23] A. Smýkalová, K. Foniok, D. Cvejn, K.M. Górecki, P. Praus, The role of guanidine hydrochloride in graphitic carbon nitride synthesis, Sci. Rep. 11 (2021) 21600, https://doi.org/10.1038/s41598-021-01009-8.
[24] H. Che, G. Che, P. Zhou, C. Liu, H. Dong, C. Li, N. Song, C. Li, Nitrogen doped carbon ribbons modified g-C_3N_4 for markedly enhanced photocatalytic H_2-production in visible to near-infrared region, Chem. Eng. J. 382 (2020) 122870, https://doi.org/10.1016/j.cej.2019.122870.
[25] Y. Li, H. Xu, S. Ouyang, D. Lu, X. Wang, D. Wang, J. Ye, In situ surface alkalinized g-C_3N_4 toward enhancement of photocatalytic H_2 evolution under visible-light irradiation, J. Mater. Chem. A 4 (2016) 2943–2950, https://doi.org/10.1039/C5TA05128B.
[26] Z. Zhu, W. Fan, Z. Liu, H. Dong, Y. Yan, P. Huo, Construction of an attapulgite intercalated mesoporous g-C3N4 with enhanced photocatalytic activity for antibiotic degradation, J. Photochem. Photobiol. A 359 (2018) 102–110, https://doi.org/10.1016/j.jphotochem.2018.04.003.
[27] Y. Zhou, W. Lv, B. Zhu, F. Tong, J. Pan, J. Bai, Q. Zhou, H. Qin, Template-free one-step synthesis of g-C_3N_4 nanosheets with simultaneous porous network and S-doping for remarkable visible-light-driven hydrogen evolution, ACS Sust. Chem. Eng. 7 (2019) 5801–5807, https://doi.org/10.1021/acssuschemeng.8b05374.
[28] C. Wang, H. Zhang, F. Li, L. Zhu, Degradation and mineralization of bisphenol A by mesoporous Bi_2WO_6 under simulated solar light irradiation, Environ. Sci. Technol. 44 (2010) 6843–6848, https://doi.org/10.1021/es101890w.
[29] N. Mzimela, S. Tichapondwa, E. Chirwa, Visible-light-activated photocatalytic degradation of rhodamine B using WO_3 nanoparticles, RSC Adv. 12 (2022) 34652–34659, https://doi.org/10.1039/D2RA06124D.
[30] Y. Li, Y. Sun, F. Dong, W.-K. Ho, Enhancing the photocatalytic activity of bulk g-C_3N_4 by introducing mesoporous structure and hybridizing with graphene, J. Colloid Interf. Sci. 436 (2014) 29–36, https://doi.org/10.1016/j.jcis.2014.09.004.
[31] X. Yang, Z. Tian, Y. Chen, H. Huang, J. Hu, B. Wen, In situ synthesis of 2D ultrathin cobalt doped g-C_3N_4 nanosheets enhances photocatalytic performance by accelerating charge transfer, J. Alloys Compd. 859 (2021) 157754, https://doi.org/10.1016/j.jallcom.2020.157754.
[32] L. Liang, L. Shi, F. Wang, L. Yao, Y. Zhang, W. Qi, Synthesis and photo-catalytic activity of porous g-C_3N_4: promotion effect of nitrogen vacancy in H_2 evolution and pollutant degradation reactions, Int. J. Hydrogen Energy 44 (2019) 16315–16326, https://doi.org/10.1016/j.ijhydene.2019.05.001.
[33] T.-B. Nguyen, C.P. Huang, R. Doong, C.-W. Chen, C.-D. Dong, Visible-light photodegradation of sulfamethoxazole (SMX) over Ag-P-codoped g-C3N4 (Ag-P@UCN) photocatalyst in water, Chem. Eng. J. 384 (2020) 123383, https://doi.org/10.1016/j.cej.2019.123383.
[34] T. Hao, S. Sun, H. Xu, H. Yu, W. Cao, G. Shao, B. Fan, H. Wang, H. Lu, Significant enhancement of photocatalytic performance by constructing porous g-C3N4 composed of nanosheets, Res. Chem. Intermed. 49 (2023) 2827–2842, https://doi.org/10.1007/s11164-023-05030-6.
[35] J. Xu, L. Zhang, R. Shi, Y. Zhu, Chemical exfoliation of graphitic carbon nitride for efficient heterogeneous photocatalysis, J. Mater. Chem. A 1 (2013) 14766–14772, https://doi.org/10.1039/C3TA13188B.
[36] U.G. Akpan, B.H. Hameed, Parameters affecting the photocatalytic degradation of dyes using TiO_2-based photocatalysts: a review, J.hazard.mater 170 (2009) 520–529, https://doi.org/10.1016/j.jhazmat.2009.05.039.
[37] C. Wen, D. Li, J. Zhong, Z. Wang, S. Huang, H. Liu, J. Wu, P. Chen, W. Lv, G. Liu, In Situ Synthesis of S-Scheme AgBr/BiOBr for Efficient Degradation of Sulfonamide Antibiotics: Synergistic Effects of Oxygen Vacancies and Heterojunctions Promote Exciton Dissociation 450 (2022) 138075, https://doi.org/10.1016/j.cej.2022.138075.
[38] Z. Lin, Y. Wu, X. Jin, D. Liang, Y. Jin, S. Huang, Z. Wang, H. Liu, P. Chen, W. Lv, G. Liu, Facile synthesis of direct Z-scheme UiO-66-NH2/PhC2Cu heterojunction with ultrahigh redox potential for enhanced photocatalytic Cr(VI) reduction and NOR degradation, 443 (2023) 130195. https://doi.org/10.1016/j.jhazmat.2022.130195.

[39] R. Mugumo, E. Ichipi, S.M. Tichapondwa, E.M.N. Chirwa, Visible-light-induced photocatalytic degradation of rhodamine B dye using a CuS/ZnS p-n heterojunction nanocomposite under visible-light irradiation, Catalysts 13 (2023), https://doi.org/10.3390/catal13081184.
[40] S. Ye, M. Yan, X. Tan, J. Liang, G. Zeng, H. Wu, B. Song, C. Zhou, Y. Yang, H. Wang, Facile assembled biochar-based nanocomposite with improved graphitization for efficient photocatalytic activity driven by visible light, Appl. Catal. B 250 (2019) 78, https://doi.org/10.1016/j.apcatb.2019.03.004.
[41] B. Zhu, P. Xia, W. Ho, J. Yu, Isoelectric point and adsorption activity of porous g-C3N4, Appl. Surf. Sci. 344 (2015) 188, https://doi.org/10.1016/j.apsusc.2015.03.086.
[42] C. Ai, D. Zhou, Q. Wang, X. Shao, Y. Lei, Optimization of operating parameters for photocatalytic degradation of tetracycline using In2S3 under natural solar radiation, Sol. Energy 113 (2015) 34–42, https://doi.org/10.1016/j.solener.2014.12.022.
[43] J. Guo, L. Jiang, J. Liang, W. Xu, H. Yu, J. Zhang, S. Ye, W. Xing, X. Yuan, Photocatalytic degradation of tetracycline antibiotics using delafossite silver ferrite-based Z-scheme photocatalyst: pathways and mechanism insight, Chemosphere 270 (2021) 128651, https://doi.org/10.1016/j.chemosphere.2020.128651.
[44] P. Huo, X. Gao, Z. Lu, X. Liu, Y. Luo, W. Xing, J. Li, Y. Yan, Photocatalytic degradation of antibiotics in water using metal ion@TiO2/HNTs under visible light, Desalin. Water Treat. 52 (2014) 6985–6995, https://doi.org/10.1080/19443994.2013.822327.
[45] F. Chen, Q. Yang, X. Li, G. Zeng, D. Wang, C. Niu, J. Zhao, H. An, T. Xie, Y. Deng, Hierarchical assembly of graphene-bridged Ag3PO4/Ag/BiVO4 (040) Z-scheme photocatalyst: An efficient, sustainable and heterogeneous catalyst with enhanced visible-light photoactivity towards tetracycline degradation under visible light irradiation, Appl. Catal. B 200 (2017) 330–342, https://doi.org/10.1016/j.apcatb.2016.07.021.
[46] Z. Lin, Z. Xiao, Y. Liu, Y. Wang, S. Chen, J. Zhang, Y. Chen, X. Zhang, G. Zhang, D. Li, W. Lv, P. Chen, G. Liu, Insights into copper(I) phenylacetylide with in-situ transformation of oxygen and enhanced visible-light response for water decontamination: Cu–O bond promotes exciton dissociation and charge transfer, 671 (2024) 1–14. <https://doi.org/10.1016/j.jcis.2024.05.159>.
[47] X. Li, Y. Chen, Y. Tao, L. Shen, Z. Xu, Z. Bian, H. Li, Challenges of photocatalysis and their coping strategies, Chem. Catal. 2 (2022) 1315–1345, https://doi.org/10.1016/j.checat.2022.04.007.
[48] S. Panneri, P. Ganguly, B.N. Nair, A.A.P. Mohamed, K.G. Warrier, U.N.S. Hareesh, Copyrolysed C3N4-Ag/ZnO ternary heterostructure systems for enhanced adsorption and photocatalytic degradation of tetracycline, Eur. J. Inorg. Chem. 2016 (2016) 5068–5076, https://doi.org/10.1002/ejic.201600646.
[49] L. Song, T. Zhao, D. Yang, X. Wang, X. Hao, Y. Liu, S. Zhang, Z.-Z. Yu, Photothermal graphene/UiO-66-NH2 fabrics for ultrafast catalytic degradation of chemical warfare agent simulants, J. Hazard. Mater. 393 (2020) 122332, https://doi.org/10.1016/j.jhazmat.2020.122332.